ADVANCED OPTICAL MATERIALS
www.advopticalmat.de

Controlled Alloying of Au@Ag Core–Shell Nanorods Induced by Femtosecond Laser Irradiation

Guillermo González-Rubio, Pablo Díaz-Núñez, Wiebke Albrecht, Vanesa Manzaneda-González, Luis Bañares, Antonio Rivera, Luis M. Liz-Marzán, Ovidio Peña-Rodríguez, Sara Bals,* and Andrés Guerrero-Martínez**

Bimetallic nanoparticles display unique physical and chemical properties, including improved chemical stability, enhanced optical properties, or higher catalytic activity. Here, a synthetic methodology is described to obtain bimetallic heterostructures and alloyed plasmonic nanocrystals through the irradiation of colloidal Au@Ag core–shell nanorods (Au@Ag NRs) with femtosecond laser pulses. Depending on the energy deposited on the Au@Ag NRs, different morphologies and degrees of alloying are obtained, such as hot-dog-like and rice-like (partially alloyed) NRs, as well as fully alloyed nanospheres. By using advanced electron microscopy techniques and energy-dispersive X-ray spectroscopy (EDX) tomography, both the morphology and the elemental distribution of the irradiated nanoparticles can be disclosed, and correlated to detailed investigations of their optical properties using electromagnetic simulations. The wide variety of bimetallic species provided by the proposed approach is a clear indication of the potential of combining synthetic colloidal methods with fs-pulsed laser irradiation for the fabrication of unique multielemental nanoparticles. The resulting control over size and composition raises promising prospects for catalytic, plasmonic, and magnetic applications of multimetallic nanocrystals.

1. Introduction

The discovery of metal alloys during the Bronze Age represents one of the most significant breakthroughs in human history, enabling the fabrication of sophisticated tools and the evolution of ancient societies into more advanced cultures. Today, alloys are essential components in innumerable materials and structures such as buildings, airplanes, computers, or medical implants. The allure of alloys stems from the improved mechanical properties (e.g., ductility or hardness) and enhanced chemical behavior (e.g., oxidation resistance) that can emerge from the combination of two or more metals.[1] In nanotechnology, the formation of alloy nanocrystals promotes drastic changes in their optical, electrical, and magnetic features and/or their performance as catalysts.[2–8] However, most of these attributes are susceptible to subtle variations in the size, shape, and composition of the nanoparticles, thereby compromising their practical application. Thus, achieving control over the alloying process and nanocrystal growth would provide a great potential in this direction. Among the wide variety of available synthetic methods, colloid chemistry is highly versatile in terms of nanoparticle shape and composition, in particular for noble metals such as platinum, silver, palladium, or gold.[9–13] For example, different kinds of mesoporous alloy nanoparticles have been synthesized using this method.[14–16]

The synthesis of colloidal alloy nanocrystals is typically accomplished via co-reduction or thermal decomposition of suitable metal precursors.[9–13,17–21] Other strategies based

Dr. G. González-Rubio, V. Manzaneda-González, Prof. L. Bañares, Prof. A. Guerrero-Martínez
Departamento de Química Física
Universidad Complutense de Madrid
Avenida Complutense s/n, Madrid 28040, Spain
E-mail: aguerrero@quim.ucm.es

Dr. G. González-Rubio, Prof. L. M. Liz-Marzán
CIC biomaGUNE
Basque Research and Technology Alliance (BRTA)
Paseo de Miramón 182, Donostia-San Sebastián 20014, Spain

Dr. P. Díaz-Núñez, Prof. A. Rivera, Prof. O. Peña-Rodríguez
Instituto de Fusión Nuclear "Guillermo Velarde,"
Universidad Politécnica de Madrid
José Gutiérrez Abascal 2, Madrid E-28006, Spain
E-mail: ovidio.pena@upm.es

The ORCID identification number(s) for the author(s) of this article can be found under https://doi.org/10.1002/adom.202002134.

Dr. W. Albrecht, Prof. S. Bals
EMAT and NANOlab Center of Excellence -University of Antwerp
Groenenborgerlaan 171, Antwerp B-2020, Belgium
E-mail: sara.bals@uantwerpen.be

Prof. L. M. Liz-Marzán
Ikerbasque (Basque Foundation for Science)
Bilbao 48013, Spain

Prof. L. M. Liz-Marzán
Department of Applied Chemistry
University of the Basque Country (EHU-UPV)
Donostia-San Sebastián 20018, Spain

DOI: 10.1002/adom.202002134

on the concurrence of seed-mediated growth methods with Galvanic replacement reactions have also been successfully employed.[9,22–25] Indeed, they allow for a better control over the resulting morphology, enabling the fabrication of hollow nanostructures (uniquely suited for catalytic applications due to their large surface area).[22,24,26] Notwithstanding, significant limitations are still present when colloidal strategies are applied, which restrict the formation of metal alloys when compared to those available in the bulk scale. For instance, the differences in the reduction potential of different metals impair the co-reduction process, often resulting in core–shell architectures rather than alloys, or involve complex and multistep procedures that hamper their scalability.[9,13] Alternative methods, such as thermal treatment of the metal precursors or of metal oxide nanoparticles in reducing environments, are widely used to prepare multimetallic alloy nanoparticles.[27–29] However, the control achieved over the morphology and size of the nanocrystals is largely limited.

Recent strategies to overcome current limitations have focused on the synthesis of bimetallic core–shell nanostructures using colloidal methods, with subsequent annealing to induce the alloying process.[30–33] This strategy provides a simple handle to control the nanoparticle composition, by tuning the relative dimensions of the core and shell. While this strategy may hold a good potential for the synthesis of colloidal alloy nanocrystals, few examples can be found in the literature. One of the reasons for its poor implementation is likely related to the need to carry out the alloying process in the dry state (i.e., where atomic diffusion is enhanced and the metals may melt together). Thus, unless the nanoparticles are protected with an additional protective shell (e.g., silica), the nanocrystals can be readily sintered and reshaped during the alloying event, thereby losing their functionality.[30]

To address these issues, we propose the synthesis of colloidal alloy nanoparticles directly in solution, where femtosecond (fs) laser irradiation emerges as the key feature enabling the alloying process without affecting the dispersion in size and shape of the nanoparticles. Plasmonic Au@Ag core–shell nanoparticles are excellent candidates to investigate this hypothesis, as they can actively interact with fs-laser pulses (owing to their ability to sustain tunable localized surface plasmon resonances, LSPRs) and thereby be heated and alloyed directly in solution.[34–39] Interestingly, this process should occur at the subnanosecond scale, without significant heating of the bulk solution, which would further help preserve the colloidal stability of the nanoparticles.[34] Hence, we first synthesized plasmonic Au@Ag nanorods (Au@Ag NRs) with a longitudinal LSPR band centered at 800 nm, in resonance with the wavelength of a 50-fs-pulsed Ti:Sapphire laser, used to investigate the proposed hypothesis. It should be noted that, the ability of Au and Ag to form alloys with different morphologies and compositions is an essential advantage of the selected system.[40]

2. Results and Discussion

The synthesis of Au@Ag NRs with an LSPR band at 800 nm started from the growth of single-crystal gold nanorods (Au NRs) with a longitudinal LSPR band at 1000 nm (see the Experimental Section and Figure S1, Supporting Information), followed by overgrowth of an Ag shell, which resulted in a blueshift of the longitudinal LSPR to 800 nm.[41–43] Indeed, by tuning the dimensions of the Ag shell, we can control the position of the longitudinal plasmon band to match the fs-laser wavelength (**Figure 1**A,B). For Au NRs of 102 ± 8 nm in length and 18 ± 2 nm in width, the growth of an Ag shell of 6 ± 2 nm in thickness at the sides was appropriate to shift the LSPR band from 1000 down to 800 nm (Figure 1A,B and Figure S1, Supporting Information). The parallelepiped-like morphology adopted by the Au@Ag NRs (108 ± 10 nm in length and 30 ± 3 nm in width, Figure 1B and Figure S2, Supporting Information) has been ascribed to the stabilization of {100} Ag facets in the presence of cetyltrimethylammonium chloride (CTAC), the surfactant used during the growth process (see the Experimental Section).[44] CTAC was further used as the colloidal stabilizing agent during the irradiation experiments.[45]

With the aim of determining the optimal conditions to trigger alloy formation, we explored the use of fs-laser pulses at different fluences, as this is the most relevant parameter to control energy deposition.[34,38,39,45,46] By varying the laser fluence, it is possible to reshape, melt, or even disintegrate plasmonic metal nanoparticles. Upon irradiation at a fluence of 3.2 J m^{-2} for 20 min (complete modification of the LSPRs), we observed a 60 nm blueshift of the Au@Ag NR longitudinal LSPR band

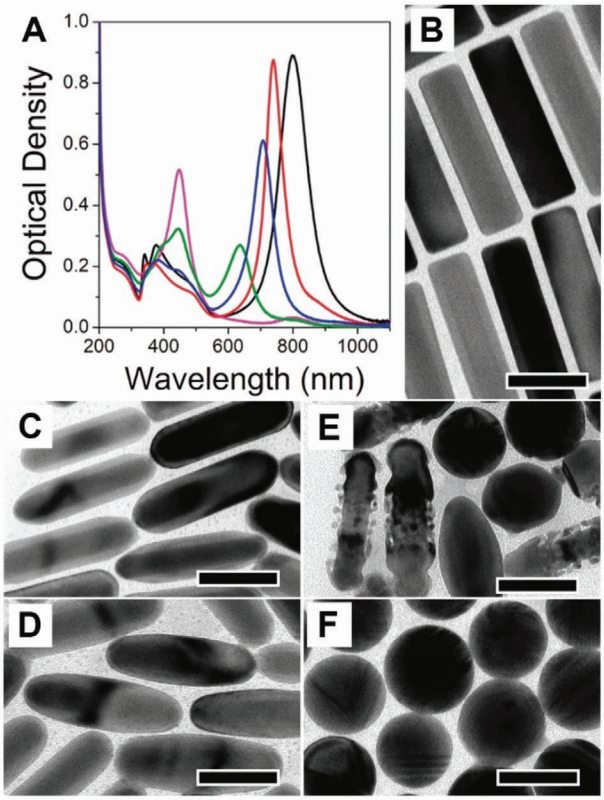

Figure 1. Effects of the pulse fluence of a fs-laser on Au@Ag NRs. A) UV–vis–NIR spectra and B–F) corresponding TEM images of Au@Ag NRs; B) before irradiation (corresponds to the black curve in (A)), and after irradiation at different fluences and times: C) 3.2 J m^{-2} for 20 min (red), D) 6.4 J m^{-2} for 10 min (blue), E) 33.28 J m^{-2} for 5 min (green), and F) 92 J m^{-2} for 2 min (magenta). Scale bars: 50 nm.

(i.e., from 800 to 740 nm, Figure 1A). Such an effect has also been observed for Au NRs irradiated with fs-laser pulses and is typically associated with a reduction of NR anisotropy.[34,46,47] However, a different morphological change was revealed upon analysis of TEM images. In the case of Au@Ag NRs, the shape of the tips was significantly modified (Figure 1C and Figure S3, Supporting Information), becoming more rounded. We additionally noticed a reduction of the Au@Ag NR length from 108 to 102 nm whereas the thickness was barely reduced (the observed 0.5–1 nm reduction can be attributed to intrinsic errors that are made during measurements of TEM images). These results suggest that the excitation of Au@Ag NRs with fs-laser pulses induces their reshaping, yielding nanoparticles with a hot-dog-like morphology. It is worth noting that a certain dispersion in the shell shape was observed for the obtained hot-dog-like NRs, which may result from two different effects. First, the energy absorbed by the NR is largely dependent on its orientation with respect to the polarization of the incident laser pulse,[34] meaning that identical rods can absorb very different amounts of energy in each pulse. Second, although to a lesser extent, dispersion in the aspect ratio of the synthesized Au@Ag NRs can also lead to varying absorption coefficients for the fs-laser wavelength. For instance, NRs with an aspect ratio larger than 3.4 will not resonate with the 800 nm fs-laser, and therefore will be modified to a lesser extent (Figure S3, Supporting Information). In both cases, the difference in absorbed energy translates into different degrees of shape modification (aspect ratio dispersion of 10–15%).

By increasing the pulse fluence to 6.4 J m^{-2}, irradiation for 10 min (complete modification of the LSPRs) induced a blueshift of the plasmon band to 710 nm. TEM analysis revealed the formation of different nanostructures such as "naked" Au NR cores (i.e., with partial or total loss of the Ag shell) and hot-dog-like NRs. In addition, NRs with a rice-like morphology (94 ± 10 nm in length and 34 ± 4 nm in width, Figure 1A,D and Figure S4, Supporting Information) and an aspect ratio of 2.8 were also observed. Further reshaping of the Au@Ag NRs was achieved by increasing the laser fluence to 33.28 J m^{-2}. Under such irradiation conditions, the longitudinal LSPR band decreased in intensity and blueshifted by ≈200 nm in less than 5 min (complete modification of the LSPRs). TEM characterization of this sample revealed the presence of nanoparticles with various morphologies (Figure 1E and Figure S5, Supporting Information), ranging from rice-like NRs with completely or partially degraded Ag shells and "naked" Au NRs, to spherical nanocrystals (NSs).

Besides the effect of size polydispersity in the irradiated Au@Ag NRs, such a broad distribution of shapes obtained at pulse fluences of 6.4 and 33.28 J m^{-2} highlights the importance of the amount of energy absorbed by each Au@Ag NR during a single laser pulse, on the subsequent evolution of the overall system. The total energy placed on an Au@Ag NR depends on the absorption cross-section at the laser wavelength, which varies as a function of both the NR orientation with respect to the laser polarization and its aspect ratio. Moreover, a substantial modification of the Au@Ag NR shape can occur at high fluences, even after a single pulse, inducing a change in the optical properties, reducing its absorption cross-section at the laser wavelength and therefore reducing also the probability of further reshaping when a second pulse arrives (i.e., the Au@Ag NR may not be any longer in resonance with the 800 nm fs-laser).[34] For example, the maximum deposition of energy occurs when the Au@Ag NR is perfectly aligned with the laser polarization. In this case, larger morphological changes may occur within a single pulse. However, if the Au@Ag NR is not well oriented, several pulses may be needed to induce significant morphological changes, which could be very different from those occurring in a single pulse. Hence, an array of morphologies can be observed at high pulse fluences (i.e., 33.28 J m^{-2}), simply because Au@Ag NRs are randomly oriented when dispersed in the solution.[34]

Furthermore, we noticed a new plasmon band centered at 447 nm, which could be associated with the formation of AuAg alloy nanospheres (AuAg NSs; Figure 1A), suggesting that alloying can take place if high pulse fluences are used. Thus, we further increased the pulse fluence to potentially improve the yield of species with an LSPR band at 447 nm, by ensuring that sufficient energy is deposited on Au@Ag NRs within a single pulse, regardless of their orientation. By reducing the beam area from 10 to 6 mm^2 (focused laser beam), a pulse fluence of 92 J m^{-2} was achieved, resulting in the disappearance of the Au@Ag NR LSPR band within less than 2 min (complete modification of the LSPRs) of irradiation (Figure 1A). The intensity of the previously mentioned band at 447 nm increased simultaneously, suggesting the formation of AuAg NSs in high yield.

Nevertheless, although the NR-to-NS transformation was confirmed by conventional TEM analysis (Figure 1F and Figure S6, Supporting Information), more advanced characterization techniques were required to determine whether fully alloyed AuAg NSs were formed, and to properly characterize the hot-dog- and rice-like NRs obtained at lower fluences. Through the use of high-angle annular dark-field scanning transmission electron microscopy (HAADF-STEM) and energy-dispersive X-ray spectroscopy (EDX) mapping, we characterized the location of Au and Ag elements in the Au@Ag NRs before and after irradiation at different pulse fluences (**Figure 2** and Figure S7, Supporting Information).[32]

EDX mapping of Au@Ag NRs confirmed the formation of an Ag shell around Au NRs, being ≈65–70% of the bimetallic nanostructure composed of Ag (Figure 2A and Figure S7, Table S1, Supporting Information). After 20 min of irradiation with 3.2 J m^{-2} fs pulses, the Ag shell was removed entirely from the tips, producing a hot-dog-like morphology, where only the sides of the Au NR core remained covered by an Ag shell. Characterization of this unique structure via EDX tomography confirmed that Au and Ag remained segregated after irradiation with low fluence pulses (Figure 2C,D and Figure S8, Supporting Information). However, when the pulse fluence was increased up to 6.4 J m^{-2}, characterization of the obtained rice-like NRs by HAADF-STEM and EDX revealed substantial changes in the distribution of Au and Ag (**Figure 3**A; Figures S9 and S10, Table S1, Supporting Information). For instance, Au atom concentration seems to increase at the tips of rice-like NRs, while Ag concentration rises at the sides. Yet, compared to the initial core–shell particles as well as the hot-dog-like NRs, the whole inner Au NR became thinner (Figure S11, Supporting Information). However, 2D projection images can be misleading and we therefore analyzed the 3D elemental composition by

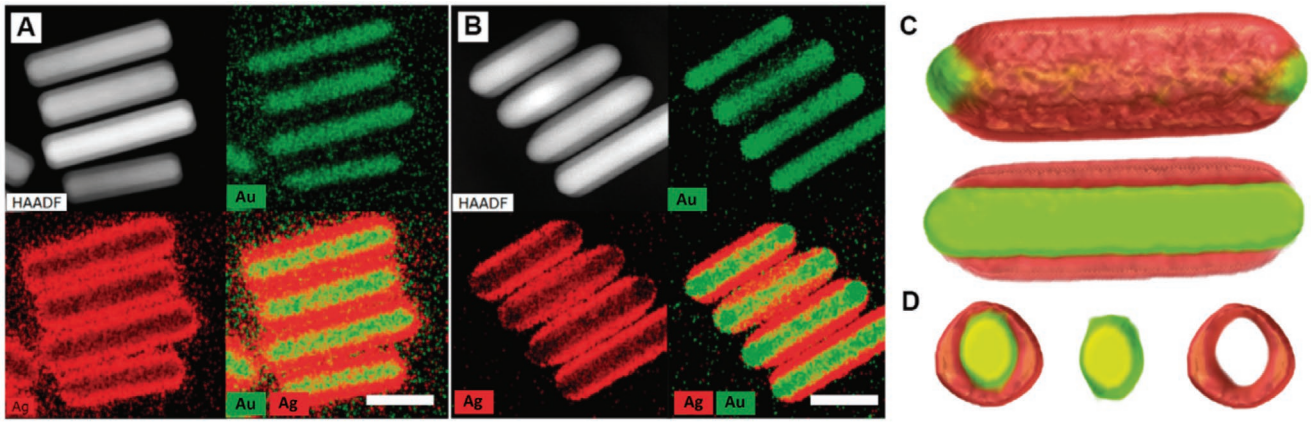

Figure 2. Morphology of Au@Ag NRs before and after irradiation with fs-laser pulses at a fluence of 3.2 J m^{-2} and characterization of the distribution of Au and Ag. A,B) HAADF-STEM images (top left) and quantified EDX maps (top right and bottom) of Au@Ag NRs A) before and B) after excitation with 3.2 J m^{-2} fs-laser pulses. Au (green, top right) and Ag (red, bottom left) atoms are clearly segregated in both cases, as it can be observed when overlapping Ag and Au maps (bottom right). C) 3D visualization of the EDX tomography (top) and D) the corresponding longitudinal section (bottom) and transversal section through the middle of the 3D reconstruction of a hot-dog-like NR, where it can be observed that Au (green) and Ag (red) are segregated. Scale bars: 50 nm.

EDX tomography. It should be noted that from pure HAADF-STEM tomography it is not possible to quantify partial alloying unless tomography was also performed under the same conditions on the very same initial nonalloyed core–shell particle.[33] From the EDX tomography reconstruction of the nanoparticles (Figure 3B) we see that, although the 2D EDX projection maps overestimate this effect, the Au core is thinner in the middle of the particle and thicker at the tips. We attribute this apparent anisotropic thinning to intermixing of Au and Ag atoms at the contact planes located in the middle region of the irradiated Au@Ag NR. This effect might be related with a higher heat power delivered in this region at the LSPR wavelength,[48,49] but further investigations would be required to confirm it. It is likely that alloying also occurred at the tips to a small extent, which lies beyond the spatial resolution of EDX tomography but might explain the overall thinning of the pure Au rod core for the rice-like particles (Figure S11, Supporting Information). These results show that alloying can be induced by fs-laser irradiation in aqueous solution (Figure 3B,C). The slight increase of Au in the tips and Ag in the middle could be explained by the diffusion of atoms toward the center of the core–shell structure. This effect would explain the overall reduction of the length observed in the rice-like NRs (i.e., 94 nm) with respect to as-synthesized Au@Ag NRs and Au NR cores (i.e., 108 and 102 nm, respectively).[34]

The formation of alloy AgAu NSs is remarkable (Figure 3D), because it suggests that the initial structures reshape and alloy within a wide range of deposited energy. In this way, the

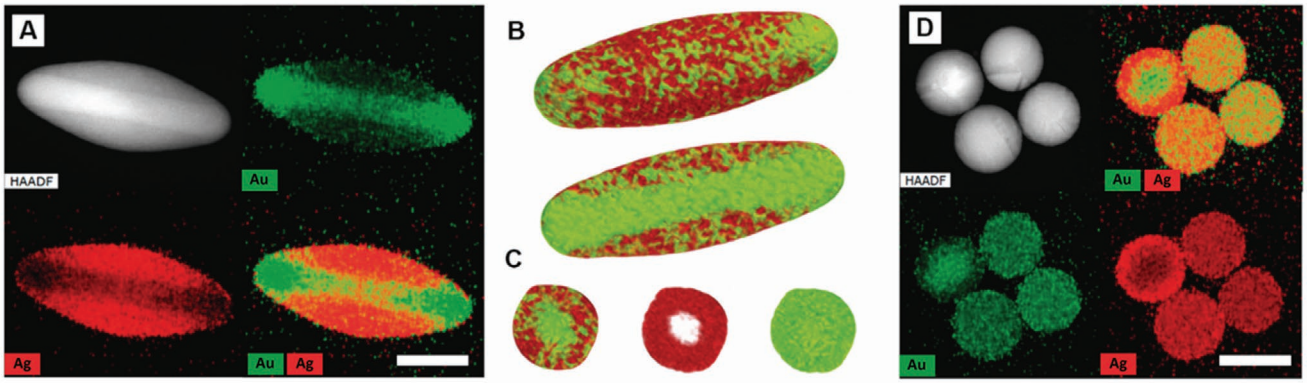

Figure 3. Morphology of Au@Ag NRs after irradiation with fs-laser pulses at fluences of 6.4 and 92 J m^{-2}, and characterization of the distribution of Au and Ag. A) HAADF-STEM image (top left) and quantified EDX maps (top right and bottom) of Au@Ag NRs after excitation with 6.4 J m^{-2} fs laser pulses. Under 6.4 J m^{-2} irradiation, Au@Ag NRs reshape into rice-like NRs, where Au from the NR core diffused into the allow, preferentially at the center, producing a slight thinning at the middle. Furthermore, Au (green) and Ag (red) atoms partially intermix, as revealed by EDX analysis (top right and bottom). B) 3D EDX tomography (top) and the corresponding longitudinal section through the middle of the 3D visualization (bottom) of a rice-like NR enable better visualization of the intermixed Au (green) and Ag (red) atoms. C) This effect can also be observed in the transversal section, where Au atoms can be seen distributed through the entire thickness. D) HAADF-STEM image (top left) and quantified EDX maps (top right and bottom) of Au@Ag NRs after excitation with 92 J m^{-2} fs-laser pulses. The initial Au@Ag NRs were transformed into alloyed spheres, where Au and Ag atoms are homogeneously mixed and distributed. Scale bars: 50 nm.

orientation of the rods with respect to the polarization of light becomes irrelevant and the pulse fluence becomes the key parameter behind the complete alloying of Au and Ag. Besides the formation of partially alloyed anisotropic nanoparticles, this strategy makes the irradiation of colloidal core-shell structures a robust method for alloy fabrication, being capable of converting the starting rods into alloyed spheres. HAADF-STEM and EDX analysis of Au@Ag NRs irradiated at an even higher pulse fluence (33.28 J m^{-2}) reinforced this idea, as we could observe the formation of AuAg NSs (i.e., a homogeneous distribution of Au and Ag with the same composition as that of the original Au@Ag NRs, between 60% and 70% of Ag). This fact might indicate that at higher fluence, the mixing of Au and Ag atoms is favored over the dissolution of the Ag shell. However, irradiation under such experimental conditions leads to a mixture of rice-like NRs, partially and completely alloyed NSs, and Au NRs with partially dissolved Ag shells (Figures S5, S12, and S13, Supporting Information). Fortunately, the efficiency of the process was largely improved when fs-laser pulses at a fluence of 92 J m^{-2} were used, as confirmed by the formation of fully alloyed AuAg NSs in a yield of over 80% (Figure 3D, Figures S6 and S14, Supporting Information).

To further understand the effect of fs-laser pulses on Au@Ag NRs, we performed a series of electromagnetic simulations. The dependence of the LSPR band on the shape and alloying degree of Au@Ag and AuAg nanoparticles provides additional means to characterize the morphology and metal atom distribution (**Figure 4**, a detailed description of the applied models and methods is provided in the Supplementary Information). To simulate the optical response of as-synthesized Au@Ag NRs, we constructed a Au NR of 102.3 × 17.8 nm covered by an Ag shell, thereby producing a parallelepiped of 108.2 × 30.4 nm (such as those characterized by HAADF-STEM, Figure 2 and Figure S15, see Supplementary Information for further details). For hot-dog-like NRs, the same Au NR core was used whereas the Ag shell was modified. A hemispherically capped cylindrical shape was adopted, with a total length of 102.3 nm and width of 30.4 nm (i.e., the same length of the Au NR core; see Figure S15, Supporting Information). In the case of rice-like NRs, on the basis of HAADF-STEM and EDX tomography, we represented them using a NR core with a slight thinning at the middle: 94 nm in length and widths of 17.8 nm at the tip and 11 nm at the center. An alloyed AuAg shell with Au and Ag content of 34% and 66%, respectively, was then employed to obtain the final rice-like morphology of 94 × 34 nm (an ellipsoidal shape, see Figures S15 and S16, Supporting Information). In all cases, the calculated longitudinal and transversal bands were close to the experimental ones. For instance, we can observe a similar blueshift of the transversal band as that experimentally seen during the formation of the hot-dog- and rice-like NRs (Figure 4A), which qualitatively proves that the simulated particles represent the geometries obtained in the irradiation experiments. Likewise, the transversal mode variation is also reflected in the simulated plasmon bands, in particular the loss of the Fano-resonance modes.[41]

Based on the simulated optical properties, the blueshift of the longitudinal band observed for the hot-dog-like NRs compared to as-synthesized ones (from 800 to 760 nm) can be explained as a result of the preferential loss of Ag from the tips and

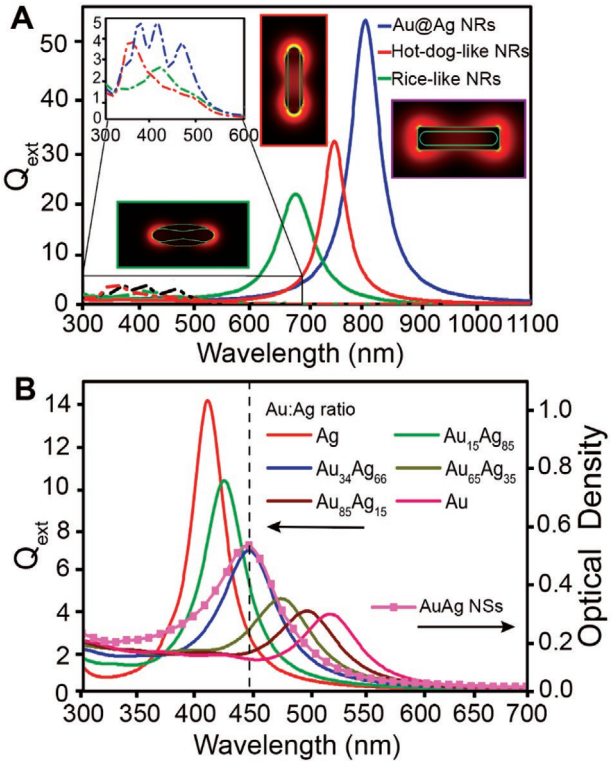

Figure 4. Optical simulations of irradiated Au@Ag NRs. A) The optical responses of as-synthesized Au@Ag NR (blue), hot-dog-like (red) and rice-like (green) NRs are shown for the longitudinal (straight lines) and transversal (dashed lines) LSPR bands. Near-field enhancement maps for the various structures are included as insets (maps are equally scaled in the range 1–80). B) The calculated optical spectra for AuAg NSs are plotted along with the experimental spectra. Dimensions of the models are given in Table S2 (Supporting Information).

modification of the cuboidal shell morphology. Indeed, these combined effects might compensate for the increase in aspect ratio, from 3.5 to 3.7. In the case of rice-like NRs, the effect of alloying was investigated. The reduction in aspect ratio might explain the large blueshift of the longitudinal LSPR band with respect to that of the as-synthesized Au@Ag NRs (from 800 to 680 nm, aspect ratio reduction from 3.5 to ≈2.8).[34,50] Moreover, its shape resembles an ellipsoid, which can further induce the observed LSPR band shift. An additional effect that might contribute to this phenomenon is the partial alloying in the shell. However, it is important to note that some discrepancies arise in the LSPR position (≈20–30 nm) between calculated and measured spectra, which can be explained by the experimentally observed alloying and morphological polydispersity. This effect is particularly relevant in rice-like NRs, which typically constitute less than 30% of the products (Figures S4 and S12, Supporting Information).

To gain further insight into the role of the morphology and degree of alloying on the LSPR position, simulations were further carried out (the results of the optical response for hot-dog- and rice-like NRs are provided in the Supplementary Information, Figures S17–S21). For hot-dog-like NRs, the Ag shell thickness and coverage of the Au NR core were varied to simulate the removal of the shell (Figure S17 and Table S2, Supporting

Information). A significant blueshift of the longitudinal LSPR band, ranging from from 770 to 725 nm, was noticed due to the reduction of the shell thickness or NR length, whereas the transversal band was barely affected. Similarly, to further understand the role of the alloying degree over the optical properties of rice-like NRs, we calculated the optical response as a function of the proportion of Au and Ag in both the core and the shell. The simulated spectra revealed that the degree of alloying does not significantly affect the LSPR position (≈620–660 nm) when it takes place in the core; however, a red-shift to 720 nm was observed when increasing the Au content in the Ag shell with a nonalloyed core (Figure S17, Supporting Information).

Near-field enhancements were also calculated for as-synthesized Au@Ag NRs and both hot-dog- and rice-like NRs. (Figure 4A and Figures S18–S21, Supporting Information). For as-synthesized Au@Ag NRs, the maximum near-field enhancement is concentrated on the edges and vertices, due to the square prism-like shape. However, for hot-dog- and rice-like NRs, the higher intensities are found at the tips, as expected due to the lack of vertices. Interestingly, the near-field enhancement intensity for both types of NRs at the plasmon wavelength is higher than that for the as-synthesized Au@Ag NRs. For hot-dog-like NRs, the electric field is significantly enhanced and concentrated at the uncovered Au NR core tips. The effect is more pronounced when increasing the amount of Ag removed from the tips (Figures S18–S20, Supporting Information), suggesting that these nanostructures may be suitable for surface-enhanced spectroscopies. This result may seem surprising, as Ag usually generates a higher field enhancement than Au, so that one would expect a reduction of the near-field enhancement. This effect may arise from the larger curvature and because the Ag shell concentrates the fields at the tips of the structure.

Finally, the theoretical optical response of AuAg alloyed NSs was also calculated.[51–54] In this case, the spectra were simulated considering a Gaussian distribution of diameters with the values obtained from TEM analysis (46 ± 3 nm). To investigate the role of the Au:Ag ratio on the optical properties, the spectra of alloyed NSs with a decreasing proportion of Ag were calculated (100%, 85%, 66%, 35%, 15%, and 0% of Ag, Figure 4B). In this case, a blue shift of the longitudinal LSPR band was observed for higher Ag contents, ranging from 525 nm for Au NSs to 400 nm for Ag NSs. Nevertheless, the resonance position of the measured optical density matches the theoretical efficiency calculated with the dielectric function for an alloy with an Ag content of 66% and Au content of 34%, which is in good agreement with the values obtained from EDX analysis. Overall, the optical simulations help us understand the effect of fs-laser pulses on the reshaping and alloying of Au@Ag NRs.

Based on the results of HAADF-STEM, EDX tomography and optical calculations, the formation of the distinct species obtained at different pulse fluences might be explained by several phenomena induced by the fs-laser. We hypothesize that the formation of hot-dog- like NRs at low fluences (3.2 J m^{-2}) arises from the loss of Ag atoms at the tips, which may result from their oxidation enhanced by laser heating and by the presence of CTAC molecules (i.e., CTAC can complex and stabilize Ag (I)) [44,55–57] The higher curvature of the tips should further facilitate this process.[58–60] At higher fluences (6.4–33.2 J m^{-2}), redistribution of Ag and Au atoms in the nanocrystal (via diffusion) and mixing (solid solution formation) are expected to occur (i.e., due to their higher activation energy). Indeed, the formation of rice-like NRs (where the shape of the as-synthesized Au@Ag NRs is strongly modified) suggests that diffusion of both Ag and Au atoms can be promoted. Moreover, partial intermixing of the different metals observed at the boundaries between the core and the shell at the middle of the Au@Ag NR implies that the pulse fluence is sufficient to induce partial alloying. In this case, we observed a reduction of the final volume and Ag content of rice-like NRs (compared to those of the as-synthesized AuNRs, from $\approx 1 \times 10^5$ to $\approx 5.7 \times 10^4$ nm^3 and ≈64%, respectively). This fact might also be explained by a partial loss of the Ag atoms due to oxidation (as hypothesized for hot-dog NRs), or due to a laser-induced fragmentation of the shell (an effect described for high-fluence fs-pulsed laser irradiation of plasmonic nanoparticles).[36–39,46,61] That could explain the presence of some irradiated Au@Ag NRs where the silver shell was partially degraded in the middle region (Figures S5 and S13, Supporting Information) or has been completely removed ("naked" NRs, Figures S4–S6, Supporting Information). Finally, at the highest investigated fluence (92 J m^{-2}), the energy absorbed by Au@Ag NRs is sufficient to induce complete reshaping and mixing (interdiffusion) of Au and Ag atoms. The size reduction (to $\approx 5.1 \times 10^4$ nm^3) suggests that part of the material constituting the as-synthesized Ag@Ag NRs is also lost. Again, we could attribute it to the loss of some Ag atoms from the shell, which would be in agreement with the slight decrease of Ag content observed in the EDX analyses (from 70% in the as-synthesized Au@Ag NRs to 64% in the AuAgNSs, Table S1, Supporting Information).

Overall, at low laser fluence oxidation of Ag might be favored. At intermediate fluences, redistribution of Ag and Au atoms in the nanocrystal could be promoted, accompanied by partial loss of Ag due to oxidation and/or fragmentation of the shell. Further increments of the lattice temperature obtained at the highest fluence could finally also induce the alloying of Ag and Au atoms.

3. Conclusions

We have described a new route to synthesize colloidal metal alloy nanoparticles, which combines wet-chemistry methods with the thermal effects produced by fs-pulsed laser irradiation. This approach involves the fabrication of bimetallic plasmonic core-shell nanoparticles, designed to efficiently absorb fs-laser pulses, thus receiving enough energy for melting to occur. Therefore, we propose that heating and subsequent alloying occur directly in the colloidal dispersion. To demonstrate this method, we synthesized core-shell Au@Ag NRs with a longitudinal LSPR band at 800 nm, in resonance with the wavelength of a 50 fs pulsed Ti:Sapphire laser. Besides the efficient plasmonic properties of Au and Ag, their ability to form a solid solution within a wide range of compositions justifies their choice as our model system. The irradiation of Au@Ag NRs at different pulse fluences was found to be critical to induce an array of effects on the shape and degree of alloying. At a fluence of 3.2 J m^{-2}, NRs with hot-dog-like morphology were obtained, where the Ag shell was partially removed under the fs-laser irradiation, with no sign of alloying. By increasing

the fluence to 6.4 J m^{-2}, rice-like NRs were formed, among other structures. Moreover, partial alloying of Au and Ag under these irradiation conditions was confirmed by HAADF-STEM imaging and EDX tomography in the case of rice-like NRs. Although this effect was more evident at fluences of 33.28 J m^{-2}, only at 92 J m^{-2} we observed complete formation of alloyed nanoparticles, which in this case adopted a spherical morphology.

We thus demonstrated a colloidal phase synthesis of AuAg nanoparticles, by irradiation of Au@Ag NRs with fs-laser pulses directly in solution. Moreover, different structures with distinct degrees of alloying can be obtained through control of the pulse fluence. Overall, the proposed strategy enables the partial and complete alloying of core-shell Au@Ag nanoparticles in a simple manner, being potentially applicable to other colloidal multimetallic heterostructures. The main requirements shall be the ability of such nanoparticles to absorb laser light (either via excitation of LSPRs or interband transitions), and the availability of fs-laser pulses with the desired wavelength and fluence. We expect this methodology to provide novel routes for the synthesis of colloidal multimetallic alloy nanoparticles with precise control over their size and composition, with prospective implications in catalytic, plasmonic, and magnetic applications. We believe that future research efforts to solve the loss of anisotropic morphology may be focused on using silica coatings, an approach that has been employed to form AuAg NRs via thermal annealing.[30,33]

4. Experimental Section

All starting materials were purchased from Sigma-Aldrich and used without further purification: hexadecyltrimethylammonium bromide (CTAB for molecular biology ≥99%), CTAC (25% w/w aqueous solution), 1-decanol (*n*-decanol, 98%), hydrogen tetrachloroaurate trihydrate ($HAuCl_4{\cdot}3H_2O$, ≥99.9%), silver nitrate ($AgNO_3$, ≥99.0%), L-ascorbic acid (≥99%), hydrochloric acid (37% weight), and sodium borohydride ($NaBH_4$, 99%) were purchased from Aldrich. MilliQ grade water (resistivity 18.2 MΩ cm at 25 °C) was used in all experiments.

Synthesis of Au@Ag NRs: The nanoparticles were prepared using an established seeded growth method with some modifications.[42]

Synthesis of Au@Ag NRs—Synthesis of 1–2 nm Au Seeds: 20 mL of a 50×10^{-3} M CTAB and 13.5×10^{-3} M *n*-decanol solution was mixed with 200 µL of 0.05 M $HAuCl_4$ and 100 µL of 0.1 M ascorbic acid solutions (stirring at ≈500 rpm and 25 and 27 °C). Once the mixture became colorless, 800 µL of a freshly prepared 0.02 M $NaBH_4$ solution was injected under vigorous stirring (1000 rpm using a PTFE plain magnetic stirring bar: 30 × 6 mm). The resulting brownish-yellow solution was aged for 1 h at 25–27 °C prior to use.

Synthesis of Au@Ag NRs—Synthesis of Small Anisotropic Seeds (21 nm in Length and 7.5 nm in Width): In a typical synthesis, 300 mL of a 50×10^{-3} M CTAB and 11×10^{-3} M *n*-decanol solution (placed in a 500 mL Erlenmeyer) was mixed with 3000 µL of 0.05 M $HAuCl_4$, 2400 µL of 0.01 M $AgNO_3$, 21 mL of 1 M HCl, and 3900 µL of 0.1 M ascorbic acid (sequentially). The solution temperature was maintained at 25 °C during the entire procedure. The growth was initiated by the addition of 18 mL of the 1–2 nm seed solution and was left to proceed undisturbed at 25 °C for at least 4 h (the solution changed from colorless to dark brownish gray during this time). The resulting small Au NRs (longitudinal LSPR located at 725–730 nm) were centrifuged at 14 000–15 000 rpm for 60 min (in 2 mL Eppendorf tubes) and redispersed with 100 mL of 10×10^{-3} M CTAB solution. This step was repeated two more times, and the small Au NR stock solution was eventually concentrated to a final value $[Au^0] = 4.65 \times 10^{-3}$ M (absorption at 400 nm of 1, optical path: 0.1 cm).

Synthesis of Au@Ag NRs—Au NRs with LSPR at 1000 nm: In a typical synthesis, 5000 µL of 0.01 M $AgNO_3$, 2000 µL of 0.05 M $HAuCl_4$, 18 000 µL of 1 M HCl, and 1600 µL of 0.1 M ascorbic acid solutions were added under stirring to 200 mL of a 50×10^{-3} M CTAB and 11×10^{-3} M *n*-decanol solution at 28 °C. The growth was initiated by the addition of 1 mL of the stock solution (under stirring). After 6 h, the Au NRs were sedimented by centrifugation at 7000 rpm, 30 min, and redispersed in 20 mL of a 25×10^{-3} M CTAC solution. This step was repeated twice to ensure the removal of CTAB. Finally, they were redispersed in 5 mL of a 25×10^{-3} M CTAC solution. The resulting Au NRs presented an average length of 102 ± 5 nm and diameter of 18 ± 2 nm.

Synthesis of Au@Ag NRs—Au@Ag NRs at 800 nm: The nanoparticles were prepared following a previously reported seeded growth method.[41] Briefly, a given volume of the Au NR solution (≈60 µL) was added to 10 mL of a 25×10^{-3} M CTAC solution (final absorption of the Au NRs in the growth mixture at 400 nm of 0.4 optical path: 1 cm). To precisely adjust the LSPR band at 800 nm, a calibration curve was previously obtained by varying the concentration of Au NRs in solution (absorption at 400 nm between 0.2 and 0.6). This concentration can vary owing to batch-to-batch fluctuations in the Au NR size and aspect ratio. Then, 500 µL of 0.01 M $AgNO_3$ and 50 µL of 0.01 M ascorbic acid solutions were added. The mixture was heated up to 65 °C and left undisturbed for 12 h. Finally, the Au@Ag NRs were centrifuged for 30 min at 5000 rpm and redispersed in 20 mL of a 25×10^{-3} M CTAC solution. This step was repeated twice.

Characterization Techniques—Transmission Electron Microscopy: TEM images were obtained on a JEOL JEM-1400PLUS transmission electron microscope operating at an acceleration voltage of 120 kV. For TEM grid preparation, 1.5 mL of the Au, Au@Ag, and irradiated products were centrifuged (in 1.5 mL Eppendorf tubes) and redispersed in 1.5 mL of a 1×10^{-3} M CTAC solution. This step was repeated twice, and the nanoparticles were redispersed in 20 µL of a 1×10^{-3} M CTAC solution. Finally, 3 µL of water and 1 µL of the nanoparticle suspension were deposited on a carbon-coated 400 square mesh copper grid (placed on Parafilm) and allowed to dry slowly.

Characterization Techniques—STEM and EDX: STEM images were acquired using a ThermoFisher Tecnai Osiris electron microscope operated at 200 kV in HAADF-STEM mode at typical beam currents of 50 pA. EDX-based elemental maps were recorded using the Super-X detector at the same microscope at typical beam currents of 150 pA and acquisition times of 10 min. All EDX maps shown were quantified representing the atomic percent of Ag and Au. For EDX tomography, a previous approach was followed as detailed elsewhere.[62,63] In short, after acquiring a HAADF-STEM tomography series in a tilt range of ±75° with an increment of 3°, EDX maps were acquired every 10° and quantified according to the ζ-factor method.[63] Both data were then combined in the reconstruction process.[62]

Characterization Techniques—UV/Vis/NIR Spectra: All experiments were carried out using a Varian Cary 5G spectrophotometer at 298 K and quartz cuvettes with optical paths of 1 cm.

Irradiation Experiments: Au@Ag NRs with longitudinal LSPR centered at 800 nm were irradiated with 50 fs, 804 nm laser pulses generated with an amplified Ti:Sapphire laser system (Spectra-Physics). Samples were irradiated in quartz cuvettes (4 mL volume, 200–2500 nm spectral range) with an optical path of 1 cm and a fixed volume of 2.5 mL (under constant stirring at 300 rpm using a magnetic bar at room temperature).

Two irradiation regimes were applied: focused and nonfocused beam irradiation. For the latter, fluence control was performed with a continuously variable neutral density filter wheel. In this case, the selected irradiation fluences were 3.2, 6.4, and 33.28 J m^{-2} with a beam diameter of about 1 cm and irradiation times of 20, 10, and 5 min, respectively. For the focused beam regime, the laser beam was focused with a 25 cm focal length silica lens, and the sample placed 10 cm from the lens to avoid damage of the cuvette. In this case, the laser fluence was 92 J m^{-2} with a beam diameter of about 6 mm and irradiation time of 2 min.

Optical Simulations: The irradiated nanoparticle optical response was studied by finite-differences in the time-domain (FDTD) using the free software computer code MEEP[64] and by Mie Theory using scattnlay

software.[51,52] The former was applied for the experimentally observed rice- and hot-dog-like NRs and the as-synthesized Au@Ag NRs,[41] whereas the latter was used for the NSs obtained at high laser fluences.

Supporting Information

Supporting Information is available from the Wiley Online Library or from the author.

Acknowledgements

G.G.-R., P.D.-N., and W.A. contributed equally to this work. This work was funded by the Spanish Ministry of Science, Innovation and Universities (MICIU) (Grant Nos. RTI2018-095844-B-I00, PID2019-105325RB, and PGC2018-096444-B-I00), the Madrid Regional Government (Grant Nos. P2018/NMT-4389 and S2018/EMT-4437), and the EUROfusion Consortium (grant ENR-IFE19.CCFE-01). This work was supported by COST (European Cooperation in Science and Technology) Action TUMIEE (Grant No. CA17126). S.B. and W.A. acknowledge funding from the European Research Council under the European Union's Horizon 2020 Research and Innovation Program (ERC Consolidator Grant No. 815128 – REALNANO). All the authors acknowledge funding from the European Commission (Grant No. E180900184-EUSMI). G.G.-R. thanks the Spanish MICIU for an FPI (Grant No. BES-2014-068972) fellowship. W.A. acknowledges an Individual Fellowship from the Marie Sklodowska-Curie actions (MSCA) under the EU's Horizon 2020 Program (Grant No. 797153, SOPMEN). The facilities provided by the Center for Ultrafast Laser of Complutense University of Madrid are gratefully acknowledged. The authors also acknowledge the computer resources and technical assistance provided by CESVIMA (UPM).

Conflict of Interest

The authors declare no conflict of interest.

Data Availability Statement

Research data are not shared.

Keywords

alloys, femtosecond pulse laser, gold, nanorods, silver

Received: December 11, 2020
Revised: February 10, 2021
Published online: March 7, 2021

[1] M. A. Benvenuto, *Metals and Alloys: Industrial Applications*, De Gruyter, Berlin **2016**.
[2] Y. Bai, C. Gao, Y. Yin, *Nanoscale* **2017**, *9*, 14875.
[3] M. B. Cortie, A. M. McDonagh, *Chem. Rev.* **2011**, *111*, 3713.
[4] T. Chen, V. O. Rodionov, *ACS Catal.* **2016**, *6*, 4025.
[5] K. Seo, N. Bagkar, S. Kim, J. In, H. Yoon, Y. Jo, B. Kim, *Nano Lett.* **2010**, *10*, 3643.
[6] J. F. Bondi, R. Misra, X. Ke, I. T. Sines, P. Schiffer, R. E. Schaak, *Chem. Mater.* **2010**, *22*, 3988.
[7] J. T. L. Gamler, H. M. Ashberry, S. E. Skrabalak, K. M. Koczkur, *Adv. Mater.* **2018**, *30*, 1801563.
[8] T. Yang, Y. L. Zhao, Y. Tong, Z. B. Jiao, J. Wei, J. X. Cai, X. D. Han, D. Chen, A. Hu, J. J. Kai, K. Lu, Y. Liu, C. T. Liu, *Science* **2018**, *362*, 933.
[9] K. D. Gilroy, A. Ruditskiy, H.-C. Peng, D. Qin, Y. Xia, *Chem. Rev.* **2016**, *116*, 10414.
[10] F. Fiévet, S. Ammar-Merah, R. Brayner, F. Chau, M. Giraud, F. Mammeri, J. Peron, J.-Y. Piquemal, L. Sicard, G. Viau, *Chem. Soc. Rev.* **2018**, *47*, 5187.
[11] Y. Xia, K. D. Gilroy, H.-C. Peng, X. Xia, *Angew. Chem., Int. Ed.* **2017**, *56*, 60.
[12] R. E. Cable, R. E. Schaak, *Chem. Mater.* **2007**, *19*, 4098.
[13] D. Wang, Y. Li, *Adv. Mater.* **2011**, *23*, 1044.
[14] H. Lv, D. Xu, L. Sun, B. Liu, *J. Phys. Chem. Lett.* **2020**, *11*, 5777.
[15] H. Lv, L. Sun, J. Feng, J. Na, D. Xu, Y. Yamauchi, B. Liu, *Chem. Commun.* **2020**, *56*, 9679.
[16] H. Lv, D. Xu, J. Henzie, J. Feng, A. Lopes, Y. Yamauchi, B. Liu, *Chem. Sci.* **2019**, *10*, 6423.
[17] R. E. Cable, R. E. Schaak, *Chem. Mater.* **2005**, *17*, 6835.
[18] R. E. Cable, R. E. Schaak, *J. Am. Chem. Soc.* **2006**, *128*, 9588.
[19] D. Wang, Y. Li, *J. Am. Chem. Soc.* **2010**, *132*, 6280.
[20] M. He, L. Protesescu, R. Caputo, F. Krumeich, M. V. Kovalenko, *Chem. Mater.* **2015**, *27*, 635.
[21] C. J. DeSantis, A. C. Sue, M. M. Bower, S. E. Skrabalak, *ACS Nano* **2012**, *6*, 2617.
[22] E. González, J. Arbiol, V. F. Puntes, *Science* **2011**, *334*, 1377.
[23] H. Jang, D.-H. Min, *ACS Nano* **2015**, *9*, 2696.
[24] Q. Zhang, J. Xie, J. Y. Lee, J. Zhang, C. Boothroyd, *Small* **2008**, *4*, 1067.
[25] L. Gan, C. Cui, M. Heggen, F. Dionigi, S. Rudi, P. Strasser, *Science* **2014**, *346*, 1502.
[26] C. Chen, Y. Kang, Z. Huo, Z. Zhu, W. Huang, H. L. Xin, J. D. Snyder, D. Li, J. A. Herron, M. Mavrikakis, M. Chi, K. L. More, Y. Li, N. M. Markovic, G. A. Somorjai, P. Yang, V. R. Stamenkovic, *Science* **2014**, *343*, 1339.
[27] Y. Yao, Z. Huang, P. Xie, S. D. Lacey, R. J. Jacob, H. Xie, F. Chen, A. Nie, T. Pu, M. Rehwoldt, D. Yu, M. R. Zachariah, C. Wang, R. Shahbazian-Yassar, J. Li, L. Hu, *Science* **2018**, *359*, 1489.
[28] P.-C. Chen, M. Liu, J. S. Du, B. Meckes, S. Wang, H. Lin, V. P. Dravid, C. Wolverton, C. A. Mirkin, *Science* **2019**, *363*, 959.
[29] D. Wang, H. L. Xin, R. Hovden, H. Wang, Y. Yu, D. A. Muller, F. J. DiSalvo, H. D. Abruña, *Nat. Mater.* **2013**, *12*, 81.
[30] W. Albrecht, J. E. S. van der Hoeven, T.-S. Deng, P. E. de Jongh, A. van Blaaderen, *Nanoscale* **2017**, *9*, 2845.
[31] Y. Ni, C. Kan, L. He, X. Zhu, M. Jiang, D. Shi, *Photonics Res.* **2019**, *7*, 558.
[32] J. E. S. van der Hoeven, T. A. J. Welling, T. A. G. Silva, J. E. van den Reijen, C. La Fontaine, X. Carrier, C. Louis, A. van Blaaderen, P. E. de Jongh, *ACS Nano* **2018**, *12*, 8467.
[33] A. Skorikov, W. Albrecht, E. Bladt, X. Xie, J. E. S. van der Hoeven, A. van Blaaderen, S. Van Aert, S. Bals, *ACS Nano* **2019**, *13*, 13421.
[34] G. González-Rubio, P. Díaz-Núñez, A. Rivera, A. Prada, G. Tardajos, J. González-Izquierdo, L. Bañares, P. Llombart, L. G. Macdowell, M. A. Palafox, L. M. Liz-Marzán, O. Peña-Rodríguez, A. Guerrero-Martínez, *Science* **2017**, *358*, 640.
[35] S. Link, M. A. El-Sayed, *Annu. Rev. Phys. Chem.* **2003**, *54*, 331.
[36] A. Pyatenko, M. Yamaguchi, M. Suzuki, *J. Phys. Chem. C* **2009**, *113*, 9078.
[37] A. Pyatenko, H. Wang, N. Koshizaki, T. Tsuji, *Laser Photonics Rev.* **2013**, *7*, 596.
[38] L. Delfour, T. E. Itina, *J. Phys. Chem. C* **2015**, *119*, 13893.
[39] J. C. Castro-Palacio, K. Ladutenko, A. Prada, G. González-Rubio, P. Díaz-Núñez, A. Guerrero-Martínez, P. Fernández de Córdoba, J. Kohanoff, J. M. Perlado, O. Peña-Rodríguez, A. Rivera, *J. Phys. Chem. Lett.* **2020**, *11*, 5108.
[40] G. Guisbiers, R. Mendoza-Cruz, L. Bazán-Díaz, J. J. Velázquez-Salazar, R. Mendoza-Perez, J. A. Robledo-Torres, J.-L. Rodriguez-Lopez, J. M. Montejano-Carrizales, R. L. Whetten, M. José-Yacamán, *ACS Nano* **2016**, *10*, 188.

[41] O. Peña-Rodríguez, P. Díaz-Núñez, G. González-Rubio, V. Manzaneda-González, A. Rivera, J. M. Perlado, E. Junquera, A. Guerrero-Martínez, *Sci. Rep.* **2020**, *10*, 5921.
[42] G. González-Rubio, V. Kumar, P. Llombart, P. Díaz-Núñez, E. Bladt, T. Altantzis, S. Bals, O. Peña-Rodríguez, E. G. Noya, L. G. MacDowell, A. Guerrero-Martínez, L. M. Liz-Marzán, *ACS Nano* **2019**, *13*, 4424.
[43] S. Gómez-Graña, J. Pérez-Juste, R. A. Alvarez-Puebla, A. Guerrero-Martínez, L. M. Liz-Marzán, *Adv. Opt. Mater.* **2013**, *1*, 477.
[44] S. Gómez-Graña, B. Goris, T. Altantzis, C. Fernández-López, E. Carbó-Argibay, A. Guerrero-Martínez, N. Almora-Barrios, N. López, I. Pastoriza-Santos, J. Pérez-Juste, S. Bals, G. Van Tendeloo, L. M. Liz-Marzán, *J. Phys. Chem. Lett.* **2013**, *4*, 2209.
[45] G. González-Rubio, T. Milagres de Oliveira, W. Albrecht, P. Díaz-Núñez, J. C. Castro-Palacio, A. Prada, R. I. González, L. Scarabelli, L. Bañares, A. Rivera, L. M. Liz-Marzán, O. Peña-Rodríguez, S. Bals, A. Guerrero-Martínez, *J. Phys. Chem. Lett.* **2020**, *11*, 670.
[46] S. Link, C. Burda, M. B. Mohamed, B. Nikoobakht, M. A. El-Sayed, *J. Phys. Chem. A* **1999**, *103*, 1165.
[47] S. Link, C. Burda, B. Nikoobakht, M. A. El-Sayed, *J. Phys. Chem. B* **2000**, *104*, 6152.
[48] G. Baffou, R. Quidant, *Laser Photonics Rev.* **2013**, *7*, 171.
[49] A. B. Taylor, A. M. Siddiquee, J. W. M. Chon, *ACS Nano* **2014**, *8*, 12071.
[50] R. Yu, L. M. Liz-Marzán, F. J. G. de Abajo, *Chem. Soc. Rev.* **2017**, *46*, 6710.
[51] O. Peña, U. Pal, *Comput. Phys. Commun.* **2009**, *180*, 2348.
[52] K. Ladutenko, U. Pal, A. Rivera, O. Peña-Rodríguez, *Comput. Phys. Commun.* **2017**, *214*, 225.
[53] O. Peña, L. Rodríguez-Fernández, V. Rodríguez-Iglesias, G. Kellermann, A. Crespo-Sosa, J. C. Cheang-Wong, H. G. Silva-Pereyra, J. Arenas-Alatorre, A. Oliver, *Appl. Opt.* **2009**, *48*, 566.
[54] V. Rodríguez-Iglesias, O. Peña-Rodríguez, H. G. Silva-Pereyra, L. Rodríguez-Fernández, G. Kellermann, J. C. Cheang-Wong, A. Crespo-Sosa, A. Oliver, *J. Phys. Chem. C* **2010**, *114*, 746.
[55] N. Almora-Barrios, G. Novell-Leruth, P. Whiting, L. M. Liz-Marzán, N. López, *Nano Lett.* **2014**, *14*, 871.
[56] M. L. Personick, C. A. Mirkin, *J. Am. Chem. Soc.* **2013**, *135*, 18238.
[57] M. R. Langille, M. L. Personick, J. Zhang, C. A. Mirkin, *J. Am. Chem. Soc.* **2012**, *134*, 14542.
[58] J. Rodríguez-Fernández, J. Pérez-Juste, P. Mulvaney, L. M. Liz-Marzán, *J. Phys. Chem. B* **2005**, *109*, 14257.
[59] M. N. O'Brien, M. R. Jones, K. A. Brown, C. A. Mirkin, *J. Am. Chem. Soc.* **2014**, *136*, 7603.
[60] G. González-Rubio, T. M. de Oliveira, T. Altantzis, A. L. Porta, A. Guerrero-Martínez, S. Bals, L. Scarabelli, L. M. Liz-Marzán, *Chem. Commun.* **2017**, *53*, 11360.
[61] G. González-Rubio, A. Guerrero-Martínez, L. M. Liz-Marzán, *Acc. Chem. Res.* **2016**, *49*, 678.
[62] D. Zanaga, T. Altantzis, L. Polavarapu, L. M. Liz-Marzán, B. Freitag, S. Bals, *Part. Part. Syst. Charact.* **2016**, *33*, 396.
[63] D. Zanaga, T. Altantzis, J. Sanctorum, B. Freitag, S. Bals, *Ultramicroscopy* **2016**, *164*, 11.
[64] A. F. Oskooi, D. Roundy, M. Ibanescu, P. Bermel, J. D. Joannopoulos, S. G. Johnson, *Comput. Phys. Commun.* **2010**, *181*, 687.